Chinese Chemical Letters 36 (2025) 110043

Contents lists available at ScienceDirect

Chinese Chemical Letters

journal homepage: www.elsevier.com/locate/cclet

An ESIPT-boosted NIR nanoprobe for ratiometric sensing of carbon monoxide *via* activatable aggregation-induced dual-color fluorescence

Min Liu[a,b,c,d,*], Bin Feng[b,d], Feiyi Chu[b,d], Duoyang Fan[b,d], Fan Zheng[b,d], Fei Chen[b,d], Wenbin Zeng[b,d,*]

[a] Department of Pharmacy, Xiangya Hospital, Central South University, Changsha 410008, China
[b] Xiangya School of Pharmaceutical Sciences, Central South University, Changsha 410013, China
[c] National Clinical Research Center for Geriatric Disorders, Xiangya Hospital, Central South University, Changsha 410008, China
[d] Hunan Key Laboratory of Diagnostic and Therapeutic Drug Research for Chronic Diseases, Changsha 410013, China

ARTICLE INFO

Article history:
Received 18 March 2024
Revised 21 May 2024
Accepted 22 May 2024
Available online 23 May 2024

Keywords:
Aggregation-induced emission
Excited-state intramolecular proton transfer
Activatable nanoprobe
Carbon monoxide
Imaging
Assessment

ABSTRACT

Carbon monoxide (CO) is a crucial gaseous signaling molecule that regulates various physiological and pathological processes, and may exert an anti-inflammatory and protective role in drug-induced liver injury (DILI). Despite this, understanding the exact relationship between CO and the occurrence and development of DILI remains challenging. Hence, there is an urgent need to develop a reliable and robust tool for the rapid visual detection and assessment of CO in this context. Herein, we presented a novel near-infrared (NIR) fluorescent nanoprobe with aggregation-induced emission (AIE) properties and excited-state intramolecular proton transfer (ESIPT) characteristics for the detection and imaging of CO both *in vitro* and *in vivo*. Simultaneously, the nanoprobe enables self-assembly form nanoaggregates in aqueous media with high biocompatible, which can sense CO *in situ* through the conversion of yellow-to-red fluorescence facilitated aggregation-induced dual-color fluorescence. What is more, this nanoprobe shows ratiometric respond to CO, which demonstrates excellent stability, high sensitivity (with a detection limit of 12.5 nmol/L), and superior selectivity. Crucially, this nanoprobe enables the visual detection of exogenous and endogenous CO in living cells and tissues affected by DILI, offering a user-friendly tool for real-time visualization of CO in living system. Hence, it holds great promise in advancing our understanding of CO's role.

The liver is the organ in the human body that is most affected by drug toxicity. That is because the liver has the primary role of converting and removing exogenous and endogenous xenobiotics from the body [1]. During the use of the drug in normal therapeutic or clinical trial dose ranges, direct or indirect liver damage of varying degrees may be caused by the drug itself or its metabolites, which is termed drug-induced liver injury (DILI). DILI ordinarily cause oxidative stress and elevated levels of reactive oxygen species (ROS) and reactive nitrogen species (RNS) [2–5], which can lead to hepatocytes necrosis and apoptosis, and ultimately to liver failure and death of the body [6,7]. Therefore, DILI is a vital key component of the review of drug marketing license applications. However, there is currently no single, definitive test for DILI. Thus, there is an urgent need to develop a desirable and robust method to diagnose the extent of DILI in living systems [8,9].

Carbon monoxide (CO) is a colorless, odorless and tasteless gas that can be lethal to humans and animals at high concentrations on account of its strong affinity for hemoglobin [10]. However, CO is also an essential gas transmitter in living organisms with cytoprotective, anti-inflammatory and signaling effects, and acts an important role in the regulation of various physiological and pathological processes [10–13]. Pieces of studies have shown that CO is an antioxidant induced by a variety of factors, such as DILI [14,15], and is mainly derived from heme oxygenase-1 (HO-1), which mediates heme catabolism in the liver [3]. Thus, endogenous CO could be somewhat representative of the health of the liver [16–19]. In this view, sensitive detection of CO levels in the liver particularly during drug-induced liver injury and repair, is of paramount importance for understanding the biological role of CO and associated pathophysiological processes.

Although some conventional techniques or methods, for instance, gas chromatography [20,21], electrochemical analysis [22,23] and colorimetric detection [24,25] have been developed for CO sensing, it is not assessable for real-time monitoring or track-

* Corresponding authors.
E-mail addresses: xyliumin@csu.edu.cn (M. Liu), wbzeng@hotmail.com, wbzeng@csu.edu.cn (W. Zeng).

https://doi.org/10.1016/j.cclet.2024.110043
1001-8417/

ing CO in living systems in a noninvasive manner. On the contrary, fluorescence-based techniques using fluorescent molecular probes are more attractive because of their advantages of high sensitivity, easy manipulation, low cost, real-time and non-invasiveness. Currently, various fluorescent molecular probes have been developed for sensing CO based on the reducibility of CO, such as the organic palladium complex [26–31], Pd^0-mediated Tsuji-Trost reaction [32–37], nitro reduction reaction [38–40] or miscellaneous [41,42].

Amongst, most such fluorescent probes for CO detection operate in turn-on mode, meaning that they only emit fluorescence when CO is present. This can be affected by several factors, such as the concentration of the probe, pH, temperature, and instrument errors. Alternatively, ratiometric probes, on the other hand, overcome these problems by self-calibrating *via* two or more emission bands. Additionally, many of the reported CO fluorescent probes suffer from aggregation-caused quenching (ACQ) properties after they accumulate in cells, which results in abnormally diminished fluorescence emission and ultimately gives rising to unsatisfactory bioimaging outcomes. In contrast, aggregation-induced emission luminogens (AIEgens) show strong emission intensity in high concentrations or the aggregation state even in aqueous solution. Ever since the concept of AIE was first put forward by Tang's group in 2001 [43], multifarious AIEgens have been developed for biosensing and bioimaging [44–46]. However, there is scarcely attempt to exploit AIE-active CO probes. To the best of our knowledge, only a few ratiometric fluorescent probes with AIE properties for CO have been reported (Table S1 in Supporting information). Therefore, there is highly demand for the demand the development of an efficient ratiometric fluorescent probe with unique AIE properties to tracke CO in biological samples.

Interestingly, excited-state intramolecular proton transfer (ESIPT), an extremely fast four-level photophysical-chemical process from enol to the keto form [47,48], is often adopted for signal regulation in probe design. Recently, several ESIPT-allowed molecules were demonstrated with AIE phenomenon and great efforts have been devoted to the relationship between AIE and ESIPT [49–51]. On the one hand, the formation of aggregates with AIE properties facilitates the emission of ESIPT, as well as helps to induce the ESIPT process with large Stokes shift, especially in solvents with high polarity or strong hydrogen-bonding donors. On the other hand, the ESIPT process promotes the formation of AIE effect through intramolecular hydrogen bonding, resulting in the enhancement of fluorescence in the aggregated state. Compared with conventional O–H-type ESIPT fluorophores, such as 2-(2′-hydroxyphenyl)benzimidazole (HBI) [52], 2-(2′-hydroxyphenyl)benzoxazole (HBO) [53], and 2-(2′-hydroxyphenyl)benzothiazole (HBT) derivatives [54], N–H-type ESIPT fluorophores typically exhibit lower but more easily adjustable ESIPT rates, making it possible to systematically adjust their fluorescence behavior from advanced dimension [55,56]. Hence, the elaborate design and synthesis of novel fluorescent probes based on N–H-type ESIPT fluorophore would be attractive and promising.

Taking the aforementioned factors into account, herein, we design and synthesized a novel nanoprobe **ABT-Ally-CO** as the reporter (Scheme 1), which possesses the significant characteristics of both the ESIPT effect and AIE feature. Then, AIE characteristic can overcome the shortcoming of ACQ; whereas ESIPT, known as a distinct four-level photochemical involving enol-keto tautomerism, thus generally exhibits a two-band emission from enol to keto, which contributes to the access to ratiometric detection. Further, the allylformate unit is introduced as the specific recognition group for CO based on the Pd^0-mediated Tsuji-Trost reaction, owing to its electron-withdrawing effect, the introduction of allylformate unit may change the electron cloud distribution of the entire fluorophore **ABT-NHTs-NH_2**, so that it provides implantation for colorimetric response to CO.

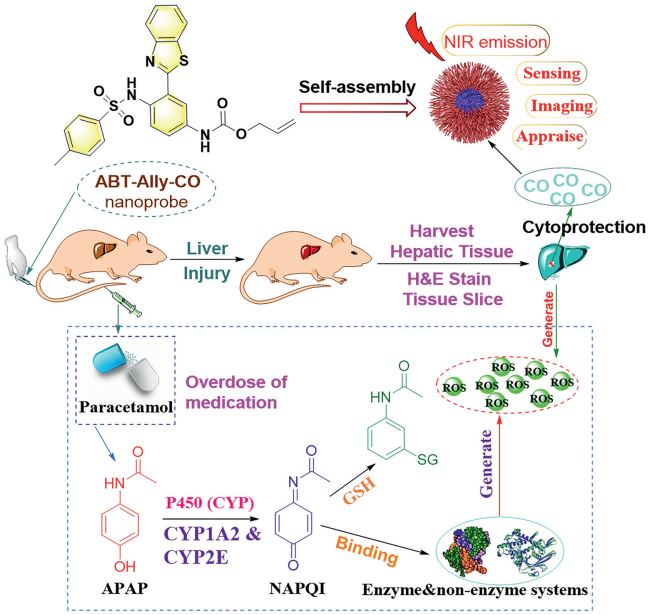

Scheme 1. The schematic illustration of the chemical structures, aggregation and dual-color imaging applications of **ABT-Ally-CO** and the potential mechanism of paracetamol (APAP)-induced liver injury producing CO.

As expected, the probe **ABT-Ally-CO** exhibited ratiometric fluorescent response toward CO, namely, the intrinsic yellow fluorescence emission (567 nm) would turn into marked red fluorescence emission (641 nm). Besides, thanks to the distinct AIE effect, CO detection was realized in aqueous media successfully. Accordingly, with desired performance *in vitro*, we further demonstrated the practicability of probe **ABT-Ally-CO** in imaging of exogenous and endogenous CO in 4T1 and HeLa cells. Finally, the applicability was validated in monitoring the upregulation of CO in DILI mice tissues successfully (Scheme 1). Therefore, the development of **ABT-Ally-CO** may provide a powerful molecular tool for accurately sensing CO *in vitro* and *in vivo*, holding the potential to diagnose and appraise of CO-associated physiological processes in living systems.

The NIR N–H-type ESIPT fluorescent probe **ABT-Ally-CO** was successfully constructed by structural modification and functionalized derivatization of 2-(2′-aminophenyl)benzothiazole *via* a five-step synthetic procedure with good yield (14.01%), and the detailed synthesis route was shown in Scheme S1 (Supporting information). In the structure, the introduction of tosyl group on the 2-position amino group of 2-(2′-aminophenyl)benzothiazole promotes the ESIPT process, while the further modification of acryl chloroformate on the 2′-phenylamino group work as the CO recognition unit, which is expected to reduce the intensity of intramolecular charge transfer (ICT) effect. Accordingly, combined with the gratifying AIE effect, the probe ABT-Ally-CO was expected to aggregate in aqueous solution with yellow fluorescence emission; once reacted with CO, the amide bond cleaved and released the fluorophore with the recovery of ICT effect within the molecule, thus showing fluorescence turned from yellow emission to red emission. With this synergistic effect in mind, we envisioned that nanoprobe **ABT-Ally-CO** could serve as accessible tool for ratiometric detection of CO.

Primarily, the photophysical-chemical properties of **ABT-Ally-CO** were investigated. As shown in Fig. S1 (Supporting information), the ultraviolet–visible (UV–vis) spectra of **ABT-Ally-CO** exhibited variation in different solvents, and the maximum absorption wavelength was prominent in *N*,*N*-dimethylformamide (DMF). Besides, based on the UV–vis spectra of **ABT-Ally-CO** in different ratios of H_2O-DMF solvent mixture (Fig. S1), the ratio of 99.5% H_2O/0.5% DMF (v/v) can be selected as the work solution, which is almost in

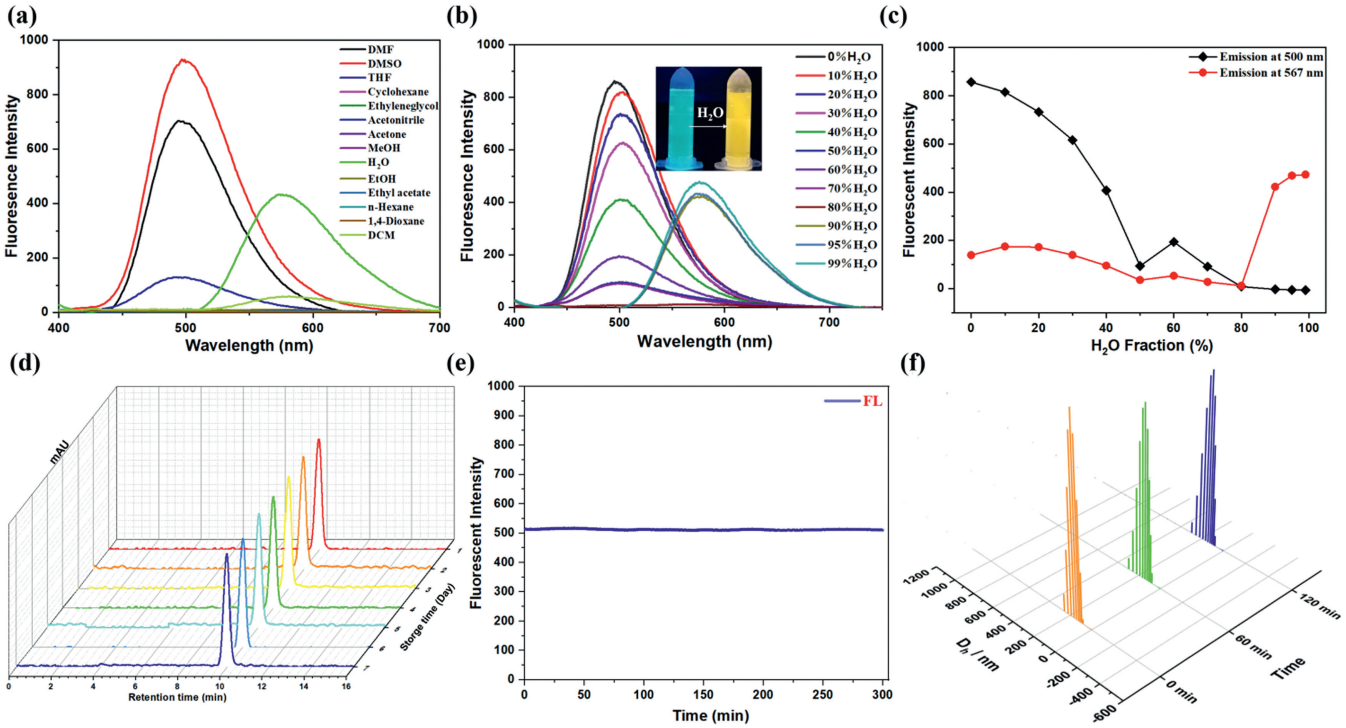

Fig. 1. (a) The emission spectrum of **ABT-Ally-CO** (10 μmol/L) in different organic solvents. (b) The emission spectrum of **ABT-Ally-CO** (10 μmol/L) in different proportions of water-DMF solvents. (c) The plots of fluorescent intensity *vs.* water fraction of **ABT-Ally-CO** at 500 nm and 577 nm. (d) The HPLC analyses of the stability for **ABT-Ally-CO**. (e) The fluorescent intensity stability of **ABT-Ally-CO** that was incubated for 12 h in the reaction buffer [10 mmol/L HEPES, 0.5% DMF] of pH 7.4 at 37 °C (characteristic absorbance band at 577 nm). (f) The DLS analyses of **ABT-Ally-CO** in water buffer solution (0.5% DMF).

aqueous media. Subsequently, the fluorescence spectra of **ABT-Ally-CO** in 99.5% H_2O/0.5% DMF (v/v) mixed solvent were also recorded, respectively. As presented in Fig. S2 (Supporting information), the maximum fluorescence spectrum was red-shifted from 500 nm to about 560 nm, showing that **ABT-Ally-CO** in almost aqueous solution forms the aggregated state which resulted in the red-shifted emission. It is noteworthy that, **ABT-Ally-CO** exhibited enamine emission less 500 nm in polar aprotic solvent such as DMF, DMSO and ACN. The phenomenon could be explained by the fact that the intermolecular hydrogen bond with solvent molecules is more competitive than intramolecular hydrogen bond, which is unfavorable for the occurrence of ESIPT process. While in H_2O, the aggregated state of **ABT-Ally-CO** is formed, the intramolecular hydrogen bond of it is strong, facilitating the occurrence of ESIPT process, leading to the imine form emission (~600 nm) (Fig. 1a). The unique solvation effect not only demonstrates the occurrence of ESIPT in **ABT-Ally-CO**, but more importantly verifies the compulsion of ESIPT upon the formation of nanoaggregates [50]. Then, the fluorescence spectrum of **ABT-Ally-CO** in different ratios of water-DMF solvents were investigated, and the results were exhibited in Fig. 1b. The fluorescence emission of **ABT-Ally-CO** at 500 nm decreased gradually with the increase of H_2O fraction, while the fluorescence emission at 567 nm increased slowly. In addition, the solvent color of **ABT-Ally-CO** changed from cyan to yellow. These results verified that ABT-Ally-CO had a significant AIE feature (Fig. 1c). It is worth mentioning that the fluorescence spectra of the fluorophore **ABT-NHTs-NH_2** at different ratios of water-DMF was also recorded, and the results were presented in Fig. S3 (Supporting information), which indicated that **ABT-NHTs-NH_2** was characterized by AIE property as well.

From the previous analysis, we have known that the process of N–H-type ESIPT occurs due to the presence of the N–H bond, thus the pH of solvent may have an enormous effect on the fluorescence. Therefore, we further evaluate the effect of pH on the sense ability of **ABT-Ally-CO**. According to Fig. S4 (Supporting information), both the probe **ABT-Ally-CO** and the fluorophore **ABT-NHTs-NH_2** displayed a similar change, the emission hypochromatic shifted with the increase of pH values. This may be explained by the fact that under alkaline conditions due to the presence of abundant -OH, the bond of N–H in the skeleton would form hydrogen bonds between the molecule and the solvent, resulting in such changes in fluorescence and solvent color; however, under strongly acidic conditions, owing to the presence of H^+, more molecular aggregates are produced and leading to the fluorescence almost drowned; while under neutral conditions, the probe was more stable, with almost no changes in the fluorescence emission, which indicates that the probe is beneficial to exert its detection and analysis role under physiological conditions.

Since **ABT-Ally-CO** is self-aggregated into a nano state under an almost aqueous solution, it is necessary to examine related properties. As shown in Fig. 1d, the high-performance liquid chromatography (HPLC) analysis showed only one chromatographic peak at retention time of about 10 min was detected with an unchanged peak area for 7 consecutive days, indicative of the excellent stability of nanoaggregate of **ABT-Ally-CO**. Consistent with this, the fluorescence intensity at maximum emission wavelength for **ABT-Ally-CO** was unchanged when it was continuously excited with 365 nm wavelength for 300 min (Fig. 1e). The dynamic light scattering (DLS, Fig. 1f) and transmission electron microscopy (TEM, Fig. S5 in Supporting information) was then applied to assess the particle size, and these results exhibited that **ABT-Ally-CO** could aggregate into nanoparticles with a size of about 200 nm, and more importantly, the nanoparticle size hardly changed within 2 h (Fig. 1f). It is worth mentioning that the nanoparticle size was positively correlated with the applied concentration of **ABT-Ally-CO** (Fig. S6 in Supporting information). The above findings demonstrated that the aggregation of **ABT-Ally-CO** into nanoparticles in aqueous solution was sufficiently stable to meet the requirements of the study.

Have validated the excellent stability of the nanoprobe, we next performed a detailed investigation of the response of **ABT-Ally-CO** to CO. As shown in Fig. S7a (Supporting information), it can be visually seen that after carbon monoxide-releasing molecule-3 (CORM-3) was added to the probe **ABT-Ally-CO** system and CO-incubation, the fluorescence color changed from yellow to red and the maximum emission wavelength shifted from 567 nm to 641 nm. What is more, the response of probe **ABT-Ally-CO** for CORM-3 was very rapid, with changes observed within 2 min and the reaction reaching equilibrium in about 30 min (Fig. S7b in Supporting information). Hence, we chose 30 min as the optimum incubation time for the following characterization. Sensitivity is an important parameter to assess the probe response to analyte. As shown in Fig. S7c (Supporting information), the fluorescence titration experiment demonstrated that the fluorescence peak at 567 nm diminished accompanied by the emergence of another fluorescence peak at 641 nm. Moreover, the fluorescence response of CORM-3 showed a good linear relationship between the fluorescence intensity ratio of I_{641}/I_{567} and COMR-3 concentration in the range of 0–40 μmol/L with $R^2 = 0.996$ (Fig. S7d in Supporting information), in other words, probe **ABT-Ally-CO** can be used for the quantitative determination of CO. The detection limit was calculated to be 12.5 nmol/L based on $3\sigma/k$, which is much lower than the most reported CO fluorescent probes (Table S1 in Supporting information). Taken together, the above results suggested that **ABT-Ally-CO** could be utilized for quantitative detection and analysis of CO with favorable sensitivity.

As a probe, high selectivity and excellent anti-interference properties are of great importance. Thus, to evaluate the selectivity of probe **ABT-Ally-CO** in the presence of various species, including active species, amino acids, biothiols and ions were investigated, as shown in Fig. S7e (Supporting information). The concentrations of all analytes were 100 μmol/L except for CORM-3 (50 μmol/L). Only in the presence of CORM-3, a new emission peak appeared at 641 nm and the solvent color changed from yellow to red, while the rest showed almost no change. When CORM-3 was contained in the systems of the above-analyzed species, the fluorescence emission at 641 nm was enhanced normally and the ratio fluorescence intensity of I_{641}/I_{567} was significantly increased as well (Fig. S7f in Supporting information). To summarize, these results indicated that **ABT-Ally-CO** had high selectivity and excellent anti-interference performance for CO sensing.

To further reveal the fluorescent mechanism, DFT and TD-DFT calculations were performed using Gaussian 16. The electrostatic potentials (ESP) of **ABT-Ally-CO** and **ABT-NHTs-NH$_2$**, were presented in Figs. 2a and b, respectively. The molecule structure based on the sulfonamide bond as the pivot axis, while the benzothiazole ring and the *p*-benzenesulfonamide unit together form an eggplant shape with an acute angle. Thus, the electronegativity of the whole molecule was focused on the sulfur and oxygen atoms of benzothiazole ring, whereas the positive charge was focused on the nitrogen atom of aniline, which portended that there was an obvious charge transfer (CT) effect in the skeleton structure of both molecules. In other words, it uncovered the significant change in the emission wavelength of **ABT-Ally-CO** in different organic solvents. Figs. 2c and d demonstrated the ESIPT four-energy level photophysical chemistry in S_0 state and S_1 state of **ABT-Ally-CO** and **ABT-NHT$_S$-NH$_2$**, respectively. That is to say, the simulations and scans were performed from an enamine structure, with N–H bond length as a function of variables, to explore the energy changes of S_0 and S_1 states. In a word, the energy levels of **ABT-Ally-CO** were overall lower than those of **ABT-NHTs-NH$_2$**, but both were susceptible to ESIPT processes. The calculated vibrational spectra of the two compounds were shown in Fig. S8 (Supporting information). In comparison, the vibrational frequencies of N–H in **ABT-Ally-CO** are larger than those in **ABT-NHTs-NH$_2$** in both S_0 and S_1 states (wave numbers of 3194.97 and 3364.58 cm^{-1} for S_0, respectively; 2506.92 and 2868.93 cm^{-1} for S_1, respectively). This could be ascribed to the fact that the allylamide structure in **ABT-Ally-CO** structure is an electron-withdrawing group, whose introduction disrupted the electron push-pull system in the backbone, further resulting in a larger vibrational frequency of the N–H bond. Next, the vertical excitation energies of both compounds were examined using the frontier molecular orbital theory. As shown in Figs. 2e and f, the $S_0 \rightarrow S_1$ excitation showed a spectrally bright state with π-π^* characteristic, which was mainly the electron transition from highest occupied molecular orbital (HOMO) to lowest unoccupied molecular orbital (LUMO). The $S_0 \rightarrow S_1$ vertical excitation energies of the two compounds were calculated as 336 nm ($f = 0.1586$) and 372 nm ($f = 0.099$), respectively, both of which were close to the experimentally measured data. However, the vertical emission energies at the TD-PBE0 level do differ from the experimental values, suggesting that the emission enhancement is accompanied by a red-shift owing to the aggregation of the compound into nanoparticles. Taken together, the excitation and emission energies of **ABT-Ally-CO** and **ABT-NHTs-NH$_2$** have been fully demonstrated by applying the TD-PBE0/def2-SVP level in combination with frontier molecular orbital theory calculations, thus confirming that the maximum excitation energy is contributed by ESIPT, while the emission energy is a joint contribution of ESIPT and AIE process.

To reveal the CO-mediated reaction process of **ABT-Ally-CO** in detail, a possible mechanism was proposed, as shown in Fig. S9 (Supporting information). In the presence of CO, Pd(II) is first reduced to Pd(0), which further forms a transition state oxide with allyl, and then, in case that the reaction equilibrium proceeds in the positive reaction direction, the transition state compound undergoes a decarbonylation to produce CO_2, thus generating **ABT-NHTs-NH$_2$**. As a result, an intense red emission could be observed in the presence of CO. To validate the idea, we traced the reaction process of **ABT-Ally-CO** with CORM-3 by HPLC (Fig. S10 in Supporting information). To further validate the proposed sensing mechanism of **ABT-Ally-CO** to CO, ultra performance liquid chromatography tandem mass spectrometry (UPLC-MS/MS) analyses were carried out. As shown in Figs. S11 and S12 (Supporting information), the HPLC profile of **ABT-Ally-CO** (2.86 min) gradually decreased while another one (1.85 min) emerged upon incubation with CO. The further high-resolution mass spectrometry (HRMS) analysis conformed the transformation from **ABT-Ally-CO** to the fluorophore **ABT-NHTs-NH$_2$** in the presence of CO**.** These results confirmed the proposed reaction mechanism.

Inspired by the favorable performance of **ABT-Ally-CO**, the feasibility of monitoring intracellular CO fluctuation in living cells was assessed. Before that, we evaluated the cytotoxicity of **ABT-Ally-CO** using a cell counting kit-8 (CCK-8) assays against 4T1 and HeLa cells, respectively. As shown in Figs. S13 and S14 (Supporting information), no obvious toxic effects (cell activity > 90%) were found even when the probe concentration was as high as 40 μmol/L, indicating its low cytotoxicity and good biocompatibility. Afterwards, the ability and applicability of **ABT-Ally-CO** in imaging of intracellular CO were verified. As shown in Figs. S15 and S16 (Supporting information), after staining with **ABT-Ally-CO** or the probe system (**ABT-Ally-CO** + $PdCl_2$) for 30 min, 4T1 cells and HeLa cells showed intensive fluorescence signals in yellow channel but faint or no signals in red channel. Upon incubation with CORM-3 (100 μmol/L) for different times (0, 10, 30 min), the signals in red channel intensified while the ones in yellow channel diminished. Foremost, the intensity ratio (I_{red}/I_{yellow}) was increased about 7-fold, so far as the increase in intensity was time-dependent.

Motivated by the above results, we further investigated the feasibility of **ABT-Ally-CO** to monitor the generation of endogenous CO in cells. It has been known that heme can induce more HO-derived CO in living cells, thus producing endogenous CO [57]. In

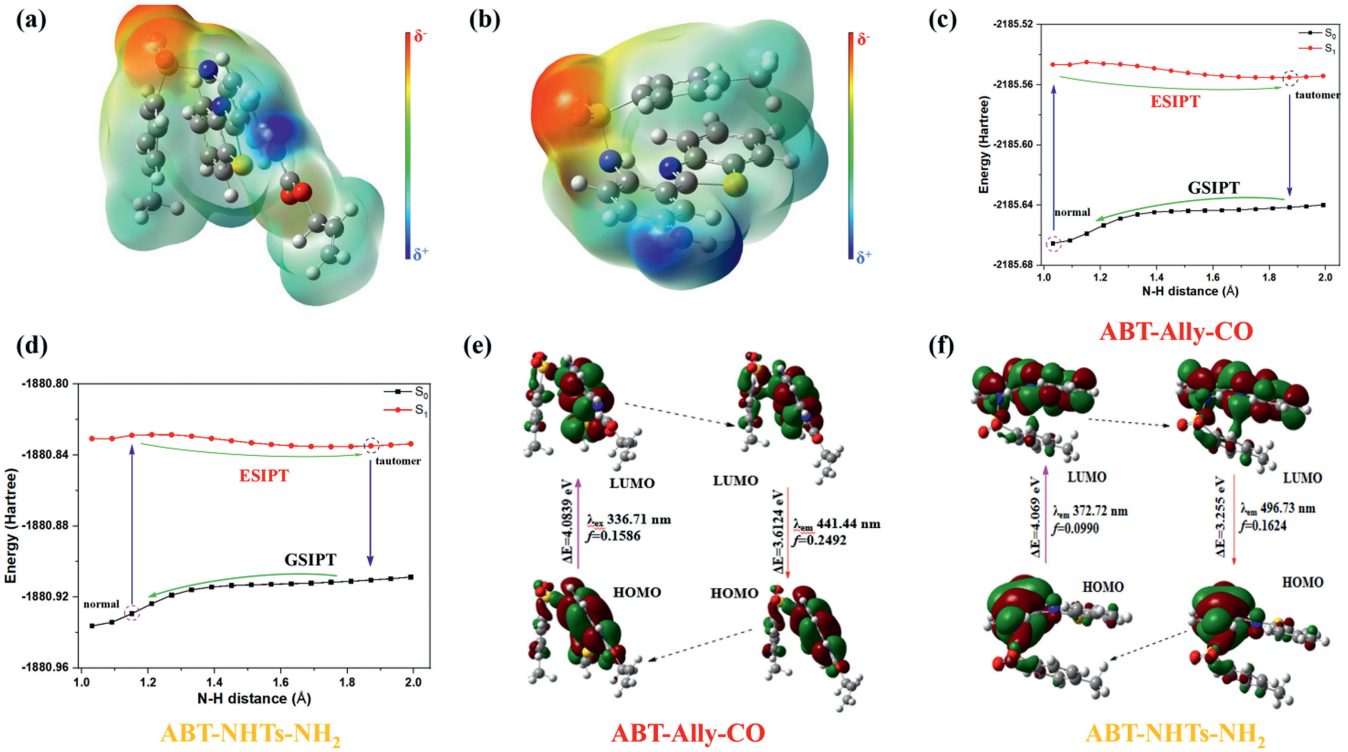

Fig. 2. The molecular electrostatic potential (MEP) of (a) **ABT-Ally-CO** and (b) **ABT-NHTs-NH$_2$**, thereinto, heatmaps represent the positive and negative potential. The energy profile of N–H distances in S_0 and S_1 for (c) **ABT-Ally-CO** and (d) **ABT-NHTs-NH$_2$**, respectively. The frontier molecular orbit theory analysis diagram for (e) **ABT-Ally-CO** and (f) **ABT-NHTs-NH$_2$** based on PBE0/def2-SVP level, respectively.

this experiment, as shown in Figs. S17 and S18 (Supporting information), 4T1 and HeLa cells were pretreated with 100 μmol/L heme for different times (0, 2, 4, 8 h), afterwards, the probe system was added to these treated cells culture medium. Upon incubation the probe system for 30 min, the laser confocal fluorescence imaging analysis was performed to record the fluorescence images. A time-dependent enhancement was observed for the signals in red channel while a progressive decrease in yellow channel. Also, the comprehensive fluorescence intensity ratio (I_{red}/I_{yellow}) of cell imaging showed a time-dependent enhancement.

In addition, lipopolysaccharide (LPS) has been reported to induce oxidative stress in cells, which may promote the generation of reducing substances for compensation [58]. Given this, the endogenous CO production during the LPS-induced oxidative stress was assessed. Firstly, 4T1 cells were pretreated with different concentrations of LPS (0, 0.5, 1.0 μg/mL) for 12 h, and then incubated with the probe system for 30 min. As shown in Fig. 3, the ratio of intracellular fluorescence intensity (I_{red}/I_{yellow}) gradually increased with increasing LPS concentration, and the dose-dependent fluorescence intensity verified the correlation between CO production and intracellular LPS concentration. What is more, the fluorescence intensity ratio (I_{red}/I_{yellow}) decreased dramatically when cells were pretreated with LPS and zinc protoporphyrin (ZnPP, HO inhibitor) for 12 h and then incubated with the probe system for 30 min. The same results can also be found in another classical tool cell, HeLa cells (Fig. S19 in Supporting information). Thus, these results suggested that the up-regulation of CO may mediate cytoprotective effects in cells under LPS stress, and equally importantly, such CO fluctuations during oxidative stress in living cells can be visualized well with **ABT-Ally-CO**. Taken together, these results demonstrated the ability of **ABT-Ally-CO** to image exogenous and endogenous CO levels in living cells.

Encouraged by the excellent performance in imaging experiments, the practical potential of **ABT-Ally-CO** was further investigated in sections of liver injury tissues. All animal experiments were performed according to the relevant ethical regulations of Xiangya Hospital, and this study received approval from Experimental Animal Ethics Committee of Xiangya Hospital, Central South University. Before that, we tested the applicability of **ABT-Ally-CO** for imaging of CO in biopsies. Normal mouse liver sections were first incubated with **ABT-Ally-CO** for 1 h and then further incubated with CORM-3 (0, 100, and 300 μmol/L), followed by laser confocal fluorescence imaging analysis on yellow and red channels. As shown in Fig. S20 (Supporting information), the emission in red channel was weak but yellow channel one was obvious in the non-CORM-3 treated tissue sections. Upon the addition of CORM-3, the emission in yellow channel was significantly weakened while the emission in red channel was gradually enhanced. Significantly, the fluorescence change was positively correlated with the concentration of CORM-3 treated. These results suggested that **ABT-Ally-CO** can be accessible for the measurement of CO in tissue.

Next, **ABT-Ally-CO** was utilized for imaging of CO fluctuations in sections of liver injury tissues. Acetaminophen (APAP) is a common drug with analgesic and antipyretic properties, but excessive APAP may lead to hepatotoxicity and induce acute liver injury with the overproduction of ROS (Scheme 1) [59]. The mice were randomly grouped into three groups and underwent different treatments (saline, APAP, and APAP + NAC (*N*-acetylcysteine)), and then the liver tissues were taken for hematoxylin-eosin (H&E) staining. As shown in Fig. 4a, the hepatocytes in the saline and APAP + NAC groups showed no obvious changes, while the hepatocytes in the APAP group showed features of liver injury such as necrosis, vacuolization and nuclear consolidation. This demonstrates that a mice model of DILI was successfully established.

Therefore, we next applied **ABT-Ally-CO** to evaluate the CO levels in liver tissue to evaluate whether the process of DILI involves increasing CO levels in hepatocytes to reduce damage to the liver in DILI mice. The experimental animals were divided into a normal

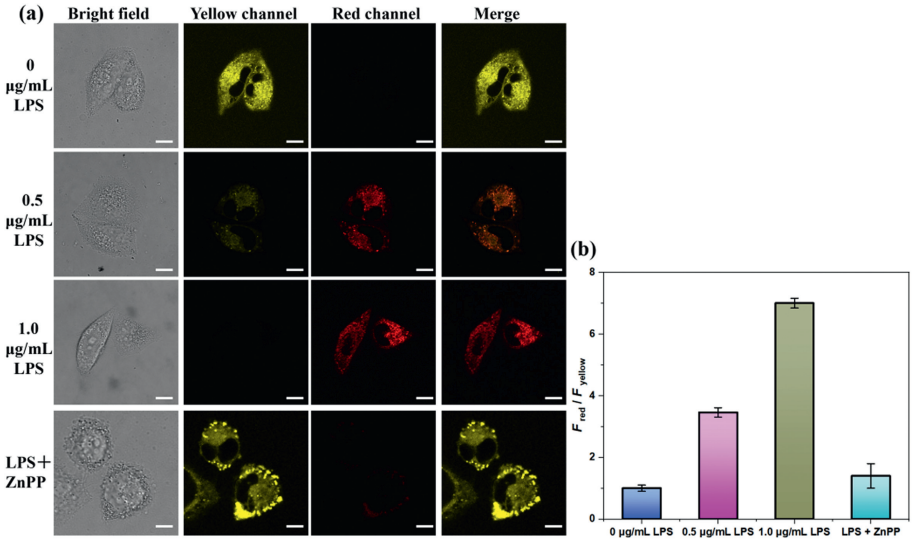

Fig. 3. Fluorescence images of endogenous CO produced by LPS stimulation in 4T1 cells. (a) The cells were pretreated with LPS (0, 0.5, 1 μg/mL) for 12 h, respectively and then cultured with the probe system (**ABT-Ally-CO** + $PdCl_2$, 10 μmol/L each) for 30 min. The other one group, firstly, the cells were pretreated with LPS (1 μg/mL) and ZnPP (10 μmol/L) for 12 h and then cultured with the probe system (**ABT-Ally-CO** + $PdCl_2$, 10 μmol/L each) for 30 min. (b) Fluorescence intensity ratios (I_{red}/I_{yellow}) of the corresponding fluorescence images in panel (a). Yellow channel: λ_{ex} = 450 nm, λ_{em} = 530–550 nm; red channel: λ_{ex} = 635 nm, λ_{em} = 650–750 nm. Scale bar: 10 μm. Data are the mean ± SD (n = 3 independent measurements).

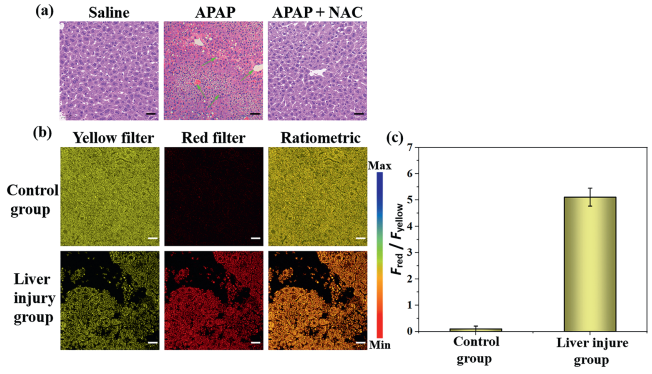

Fig. 4. (a) H&E staining of the liver slices. Scale bar: 100 μm. (b) Fluorescence microscope images of mice liver tissue sections. Scale bar: 100 μm. (c) Fluorescence intensity ratios (I_{red}/I_{yellow}) of the corresponding fluorescence images in panel (b). Yellow channel: λ_{ex} = 450 nm, λ_{em} = 530–550 nm; red channel: λ_{ex} = 635 nm, λ_{em} = 650–750 nm. Data are the mean ± SD (n = 3 independent measurements).

mice group (control group) and a DILI model mice group (liver injury group). As shown in Figs. 4b and c, compared with the liver tissue of control mice, the signal intensity in yellow channel was significantly decreased while red channel was increased in DILI group. Correspondingly, a significantly higher ratio of I_{red}/I_{yellow} emission was observed in DILI group, foreboding that the increased CO levels may act as a self-protective stress response to the liver injury. Overall, these results demonstrated that **ABT-Ally-CO** can be used for imaging CO not only in living cells but also in liver tissues.

In summary, a novel fluorescent nanoprobe **ABT-Ally-CO** was successfully designed and built for CO detection and imaging. Owing to the AIE + ESIPT synergistic effect, the probe could self-aggregate into nanoaggregates in aqueous solution with the advantage traits of NIR emission and high stability, thus can be accessible in aqueous media with excellent selectivity and good sensitivity (limit of detection = 12.5 nmol/L). With the probe in hand, CO imaging both in living cells and in DILI tissues was well performed. Through this study, we found elevated CO levels in the DILI mice and demonstrated a possible role of CO as a protective gas. More importantly, this nanoprobe is expected to be a robust biotechnological tool for *in vitro* and *in vivo* CO monitoring.

Declaration of competing interest

The authors declare that they have no known competing financial interests or personal relationships that could have appeared to influence the work reported in this paper.

CRediT authorship contribution statement

Min Liu: Writing – original draft, Project administration, Investigation, Funding acquisition, Data curation, Conceptualization. **Bin Feng:** Software, Methodology, Formal analysis. **Feiyi Chu:** Writing – review & editing, Formal analysis. **Duoyang Fan:** Writing – review & editing, Software. **Fan Zheng:** Writing – review & editing, Software. **Fei Chen:** Supervision, Data curation. **Wenbin Zeng:** Supervision, Project administration, Funding acquisition.

Acknowledgments

We sincerely appreciate the financial support by the National Natural Science Foundation of China (Nos. 82272067, 81974386, 22107123 and M-0696), the Natural Science Foundation of Hunan Province (Nos. 2021JJ41008, 2022JJ80052, 2022JJ40656, 2023JJ20077), the Key Project of Changsha Science and Technology Plan (No. kh2201059), the Scientific Research Project of Health Commission of Hunan Province (No. B202313057213), and the Youth Science Foundation of Xiangya Hospital (No. 2022Q16).

Supplementary materials

Supplementary material associated with this article can be found, in the online version, at doi:10.1016/j.cclet.2024.110043.

References

[1] M.Z. Sakatis, M.J. Reese, A.W. Harrell, et al., Chem. Res. Toxicol. 25 (2012) 2067–2082.
[2] J. Chen, D.Y. Huang, M.Y. She, et al., ACS Sens. 6 (2021) 628–640.
[3] A.J. Shuhendler, K.Y. Pu, L.N. Cui, et al., Nat. Biotechnol. 32 (2014) 373–380.

[4] T. Tian, Y.H. Ho, C. Chen, et al., Chin. Chem. Lett. 33 (2022) 3167–3171.
[5] A.K.U. Gerd, J.A. Raul, M. Michael, et al., Gut 66 (2017) 1154.
[6] S.M. Feng, Z.P. Zheng, S.Y. Gong, et al., Sens. Actuat. B: Chem. 361 (2022) 131751.
[7] D.J. Antoine, A.H. Harrill, P.B. Watkins, et al., Toxicol. Res. 3 (2014) 75–85.
[8] B.H. Norman, J. Med. Chem. 63 (2020) 11397–11419.
[9] M.J. Waring, J. Arrowsmith, A.R. Leach, et al., Nat. Rev. Drug Discov. 14 (2015) 475–486.
[10] L.K. Weaver, New Engl. J. Med. 360 (2009) 1217–1225.
[11] R. Motterlini, R. Foresti, Am. J. Physiol. Cell Physiol. 312 (2017) C302–C313.
[12] S.Y. Gong, E.B. Zhou, Y.J. Liu, et al., Anal. Chem. 94 (2022) 2042–2047.
[13] J.A. Robson, M. Kubánková, T. Bond, et al., Angew. Chem. Int. Ed. 59 (2020) 21431–21435.
[14] B. Wang, C.G. Huang, L.J. Chen, et al., ACS Biomater. Sci. Eng. 6 (2020) 798–812.
[15] T. Kyokane, S. Norimizu, H. Taniai, et al., Gastroenterology 120 (2001) 1227–1240.
[16] M.N. Ye, Q. Tan, D.T. Jiang, et al., ACS Appl. Mater. Interfaces 14 (2022) 52659–52669.
[17] B.D. Song, C. Zhang, W.R. Hu, et al., J. Control. Rel. 331 (2021) 350–363.
[18] L. Liu, J.Y. Xu, S.P. Zhang, et al., Sens. Actuat. B: Chem. 367 (2022) 132171.
[19] Y. Li, J.G. Zhang, S.M. Cheng, et al., Anal. Chem. 95 (2023) 7439–7447.
[20] G.S. Marks, H.J. Vreman, B.E. Mclaughlin, et al., Antioxid. Redox. Sig. 4 (2002) 271–277.
[21] S. Oliverio, V. Varlet, J. Chromatogr. B 1090 (2018) 81–89.
[22] L.X. Tao, Y. Kong, Y.H. Xiang, et al., Chin. Chem. Lett. 34 (2023) 107481.
[23] H.K. Kwon, M. Kim, J.P. Grote, et al., J. Am. Chem. Soc. 140 (2018) 16198–16205.
[24] S. Heylen, J.A. Martens, Angew. Chem. Int. Edit. 49 (2010) 7629–7630.
[25] M.E. Moragues, J. Esteban, J.V. Ros-Lis, et al., J. Am. Chem. Soc. 133 (2011) 15762–15772.
[26] K.B. Zheng, W.Y. Lin, L. Tan, et al., Chem. Sci. 5 (2014) 3439–3448.
[27] K.Y. Liu, X.Q. Kong, Y.Y. Ma, et al., Angew. Chem. Int. Ed. 56 (2017) 13489–13492.
[28] S. Xu, H.W. Liu, X. Yin, et al., Chem. Sci. 10 (2019) 320–325.
[29] L. Yuan, W.Y. Lin, L. Tan, et al., Angew. Chem. Int. Ed. 52 (2013) 1628–1630.
[30] S. Minegishi, A. Yumura, H. Miyoshi, et al., J. Am. Chem. Soc. 139 (2017) 5984–5991.
[31] M.T. Sun, H. Yu, K. Zhang, et al., ACS Sens. 3 (2018) 285–289.
[32] M. Liu, R.X. Xiao, B. Feng, et al., Sens. Actuat. B: Chem. 342 (2021) 130038.
[33] W.X. Li, R. Li, R. Chen, et al., Anal. Chem. 94 (2022) 7996–8004.
[34] J.G. Wang, C.B. Li, Q.Q. Chen, et al., Anal. Chem. 91 (2019) 9388–9392.
[35] W.X. Li, R. Li, R. Chen, et al., Anal. Chem. 93 (2021) 8978–8985.
[36] J.W. Zhang, Y.R. Liu, L. Jiang, et al., Sens. Actuat. B: Chem. 351 (2022) 130936.
[37] G.Q. Fu, Y.S. Xia, W.L. Jiang, et al., Talanta 243 (2022) 123398.
[38] H. Zhao, M. Wang, Z.M. Li, et al., Sens. Actuat. B: Chem. 377 (2023) 133059.
[39] S.J. Li, K. Yang, J.Y. Zeng, et al., ACS Omega 7 (2022) 9929–9935.
[40] K. Dhara, S. Lohar, A. Patra, et al., Anal. Chem. 90 (2018) 2933–2938.
[41] C. Torre, A. Toscani, C. Marín-Hernandez, et al., J. Am. Chem. Soc. 139 (2017) 18484–18487.
[42] G.C. Ma, Q.H. Ding, Y.D. Zhang, et al., Chin. Chem. Lett. 35 (2024) 109293.
[43] J.D. Luo, Z.L. Xie, J.W.Y. Lam, et al., Chem. Commun. (2001) 1740–1741.
[44] M. Liu, S.B. Zhong, B. Feng, et al., Chin. Chem. Lett. 34 (2023) 107940.
[45] Y.H. Duo, G.H. Luo, W.T. Zhang, et al., Chem. Soc. Rev. 52 (2023) 1024–1067.
[46] G.L. Niu, R.Y. Zhang, X.J. Shi, et al., Anal. Chem. 123 (2020) 115769.
[47] V.S. Padalkar, S. Seki, Chem. Soc. Rev. 45 (2016) 169–202.
[48] A.C. Sedgwick, L.L. Wu, H.H. Han, et al., Chem. Soc. Rev. 47 (2018) 8842–8880.
[49] X. Cheng, K. Wang, S. Huang, et al., Angew. Chem. Int. Ed. 54 (2015) 8369–8373.
[50] Y.H. Chen, Y. Fang, H. Gu, et al., ACS Appl. Mater. Interfaces 12 (2020) 55094–55106.
[51] S. Huang, B. Feng, X. Cheng, et al., Chem. Eng. J. 476 (2023) 146436.
[52] S. Park, O.H. Kwon, S. Kim, et al., J. Am. Chem. Soc. 127 (2005) 10070–10074.
[53] A. Ohshima, A. Momotake, R. Nagahata, J. Phys. Chem. A 109 (2005) 9731–9736.
[54] K. Li, Q. Feng, G.L. Niu, et al., ACS Sens. 3 (2018) 920–928.
[55] H.W. Tseng, J.Q. Liu, Y.A. Chen, et al., J. Phys. Chem. Lett. 6 (2015) 1477–1486.
[56] Y. Liu, A.Y. Bi, T. Gao, et al., Talanta 194 (2019) 38–45.
[57] E. Gomperts, J.D. Belcher, L.E. Otterbein, et al., Am. J. Hematol. 92 (2017) 569–582.
[58] P.R. Angelova, I. Myers, A. Abramov, Redox Biol. 60 (2023) 102598.
[59] N. Wang, H. Wang, J. Zhang, et al., Chin. Chem. Lett. 33 (2022) 1584–1588.